

Restricting alloying reaction of sns nanoparticles as negative electrode towards building high-performance lithium-ion batteries and capacitors with robust cycling

Manohar Akshay^a, Yun-Sung Lee^{b,*}, Vanchiappan Aravindan^{a,*}

^a Department of Chemistry, Indian Institute of Science Education and Research (IISER) Tirupati 517619, India

^b School of Chemical Engineering, Chonnam National University, Gwang-ju 61186, Republic of Korea

ARTICLE INFO

Keywords:

Alloy anode
Li-ion battery
Li-ion capacitor
Energy density
Durability

ABSTRACT

The lithium-ion capacitor (LIC) is a relatively new device that has emerged on the battlefield and can potentially put down the LIBs. These hybrid devices have two different electrode mechanisms (Faradaic and non-Faradaic) that bridge the gap between the LIBs and conventional supercapacitors. Herein, we introduce an appropriate electrode material, tin sulphide, SnS, which could be used as an anode in LIBs and LICs by limiting only an alloy-type reaction. This work explores the possibility of fabricating LIB and LIC with SnS nanoparticles as anode and commercial $\text{LiNi}_{0.5}\text{Mn}_{1.5}\text{O}_4$ and activated carbon (AC) as a cathode under balanced loading conditions. For the case of LIC, prior to the fabrication, the Li/SnS cell is electrochemically pre-lithiated ($\text{Li}_x\text{Sn} + \text{Li}_2\text{S}$) and paired with the cathode AC. The LIB and LIC displayed a maximum energy density of 387 and 172 Wh kg^{-1} , respectively, with ultra-long cyclability and capacity retention. The adaptability of these devices to various climatic conditions is validated by testing the full cell at different temperature conditions (-10 to 50°C). Thus, from all the studies, we discovered that the SnS could be a potential candidate that could replace the graphitic carbon anode in both Li-ion batteries and capacitor configurations.

1. Introduction

Electrochemical energy storage devices have gained great interest due to their high energy, efficient storage, scalability, and nearly zero carbon footprint after production. Lithium-ion batteries (LIBs) [1,2] and supercapacitors (SCs) [3–5] have mainly gained much attention because of their application in portable electronics, automobiles, power stations, etc. They have a leading position in the energy market because of their enhanced energy density, power values, cyclability, long-term stability, environmental friendliness, etc. The LIBs and SCs are devices with different energy storage mechanisms and complementary electrochemical performance. The former has high energy and low power density, whereas the latter has higher power and comparatively lower energy density. Lithium-ion capacitors (LICs) are hybrid devices with the properties of both LIBs and SCs and are built to fill the gap between these two prominent devices. The battery-type negative electrode provides the energy density, and the capacitive-type positive electrode improves the power characteristics of the LICs [6–9].

The negative electrode has a significant role in enhancing

electrochemical performance, particularly the energy density of both LIBs and LICs. Three major Faradaic energy storage mechanisms in anode materials include intercalation, alloying and conversion. In the earlier stages of LIB research, before the commercialization of LIB by Sony in the 1990s, intercalation-type materials such as graphite and $\text{Li}_4\text{Ti}_5\text{O}_{12}$ were in great demand, and most of the researches were pointed towards them mainly because of their stable cycling performances [10–14]. However, the increase in energy demand and the necessity for high-capacity devices made people think about materials beyond the intercalation type [15–17]. The prime reasons to explore alternatives are the low theoretical capacity, sluggish Li-ion kinetics, and limited energy density of intercalation-based materials. On the other hand, the alloying/conversion-type anode has a high theoretical capacity owing to the multi-electron reaction, higher energy density, optimal operational potential and better safety characteristics. Notably, alloying-type anodes have less polarization and irreversibility than conversion-type electrodes, making them a better type of anode material in batteries and hybrid capacitors.

There are different alloy-type anode materials, some of which are

* Corresponding authors.

E-mail addresses: leeys@chonnam.ac.kr (Y.-S. Lee), aravind.van@yahoo.com (V. Aravindan).

<https://doi.org/10.1016/j.electacta.2025.147385>

Received 22 May 2025; Received in revised form 5 September 2025; Accepted 13 September 2025

Available online 13 September 2025

0013-4686/© 2025 Elsevier Ltd. All rights are reserved, including those for text and data mining, AI training, and similar technologies.

silicon-based, germanium-based, tin-based and lead-based derivatives. The silicon and tin-based are the ones more explored because of their low-cost and non-toxic nature [17–21]. These elements form an alloy with Li^+ by the reaction: $\text{A} + x\text{Li}^+ + xe^- \rightarrow \text{Li}_x\text{A}$ ($\text{A} = \text{Sn, Si, Ge, etc.}$) results in multiple electron transfers and thereby has a higher theoretical capacity. During the alloying process, each metal atom can take up to a maximum of 4.4 mol of Li atoms to form the fully lithiated phase ($\text{Li}_{4.4}\text{A}$). However, the continuous alloying and de-alloying results in huge volume variation, pulverization of electrodes, and continuous breaking/reformation of solid electrolyte interface (SEI), leading to the deterioration of the electrochemical performance. Compared with the other elements in the group, the Sn has the least volume variation (260 % for $\text{Li}_{4.4}\text{Sn}$, 420 % for $\text{Li}_{3.75}\text{Si}$, and 370 % for $\text{Li}_{4.4}\text{Ge}$) with better gravimetric and volumetric capacity (990 mAh g^{-1} & 2020 mAh cm^{-3}). In addition, the Sn has better conductivity than the other two and a suitable lower redox potential, making it an ideal anode for batteries and hybrid capacitors [22].

This work explored the potentiality of SnS nanoparticles as an alloy-type anode for the LIB and LIC. We adopted a single-step co-precipitation method for synthesizing SnS nanoparticles in room temperature conditions. In most previous reports, the researchers have utilized the wide potential window of SnS (0.005 to 3 V vs. Li) to extract the maximum capacity by compromising the redox potential by allowing both alloying (limiting to max. of 4.4 mol of Li) and subsequent conversion reactions (overall 6.4 mol of Li). This results in huge volume variation and large polarization, leading to degradation of electrochemical performance and making it difficult to stabilize upon long-term cycling. The larger polarization eventually dilutes the net energy density, irrespective of whether it is batteries or hybrid capacitors. Hence, it is observed that most works include controlled morphological synthesis of SnS and incorporation of the dopants to achieve stabilization over cycles, controlling the volume expansion [23–25]. For example, Cheng and co-workers [26] incorporated an additional sulphur-doped carbon layer over the SnS to control the volume variation and to maintain the structural integrity. Similar work was reported by Bing Zhao *et al* [27], where they caged the SnS with a graphene bubble and used it as an anode for LIBs. On the contrary, our work adopted a simple synthesis strategy with no such modification over the SnS nanoparticle, but the redox potential is limited to only (max. of 4.4 mol of Li) the alloying reaction region (charging up to 0.8 V vs. Li) and does not allow further conversion of its native form (*i.e.* SnS). The SnS electrode paired with lithium metal displayed better long-term cycling, rate performance, and robust SEI, as evaluated from the *in-situ* EIS studies. The electrochemically pre-treated/lithiated SnS is paired with the respective cathodes ($\text{LiNi}_{0.5}\text{Mn}_{1.5}\text{O}_4/\text{activated carbon, AC}$) for the battery/capacitor assemblies, and both displayed excellent electrochemical activity and feasibility in a wide range of conditions, which are discussed in detail in the manuscript.

2. Experimental section

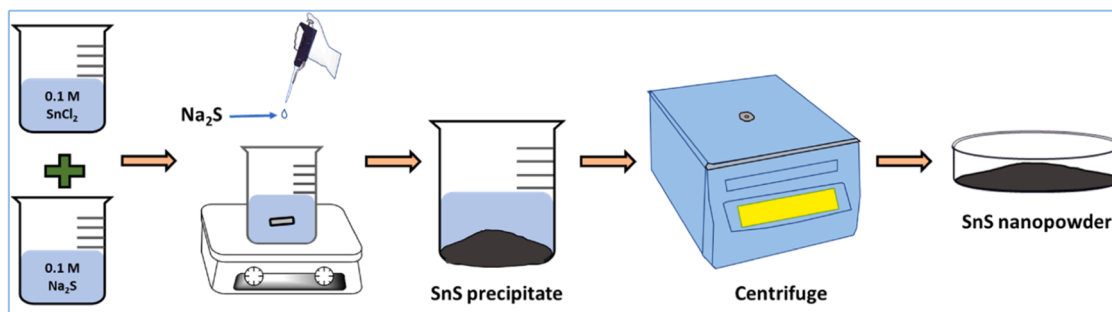
Synthesis of SnS nanoparticles: The SnS nanoparticles are synthesized using an easy single-step procedure as given in Equation E_s2 below. 0.1 M SnCl_2 is prepared by dissolving 4.74 g in 10 ml of conc. HCl followed by an addition of 240 ml of distilled water. Meanwhile, 0.1 M Na_2S is prepared in another beaker by dissolving 1.95 g in 250 ml of distilled water. After the dissolution of both, the Na_2S solution is added dropwise to the SnCl_2 solution, resulting in the formation of a brown-coloured SnS precipitate. The precipitate is collected and washed with distilled water and ethanol multiple times to remove the NaCl impurity. The SnS is then dried at 65°C and stored for further analysis. The synthesis procedure is step-by-step displayed in Scheme 1.



Material characterizations: Crystal structure and material phase formed were analyzed from the X-ray diffraction studies using Rigaku Smartlab automated multipurpose diffractometer (40 kV, 200 mA, $\lambda = 1.5406 \text{ \AA}$) with Cu K α radiation. The BET surface features, area, porosity, etc., were analyzed using an automated gas sorption analyzer (Autosorb IQ-XR-XR-XR, 3 stat., Viton). The surface elements of the sample were analyzed, and the purity was confirmed from the X-ray photoelectron spectroscopy (XPS, Multilab 2000, UK; monochromatic Al K α radiation $h\nu = 1486.6 \text{ eV}$) studies. Field-emission scanning electron microscopy (FE-SEM, Gemini 560, Germany) and high-resolution transmission electron microscopy (HR-TEM, JEM-2000, EX-II, JEOL, Japan) examined the surface morphology and internal structure of the sample. The material's qualitative and quantitative elemental composition was obtained from the energy-dispersive X-ray spectroscopy (EDS, Ametek).

Electrochemical Studies: SnS electrodes were fabricated using the slurry coating method. The SnS active material, conductive carbon (acetylene black), and binder (Tab-2) are mixed in an 8:1:1 ratio in the N-methyl pyrrolidone (NMP) solvent and kept for overnight stirring. The homogenous slurry obtained is coated over the copper foil current collector using the doctor blade apparatus (MSK-AFA-III Automatic Thick Film Coater, MTI Corporation). The coating is dried for at least four hours at 65°C in a hot air oven. After complete drying, the coating was pressed using a calendar roll (Tester Sangyo, Japan) for densification purposes, and 12 mm diameter electrodes were punched out for cell fabrication. The cathode was fabricated using a different conventional hand-made method. The activated carbon (YP 80F Kuraray, Japan; Surface area: $2100 \text{ m}^2 \text{ g}^{-1}$, Pore volume: 0.97 mL g^{-1}), acetylene black and tab-2 (with wt. % 8: 1: 1) were mixed in mortar & pestle using ethanol as the solvent. This is made into a thin free-standing film and pressed over the stainless-steel mesh (Goodfellow, UK) of 14 mm diameter using the pellet maker and hydraulic press.

The fabricated electrodes (anode and cathode) were dried at 75°C for at least four hours in a vacuum oven before the cell fabrication. All the cells were fabricated inside the argon-filled glove box workstation (MBraun, Germany) with O_2 and H_2O levels $<0.1 \text{ ppm}$. The CR2016 type coin-cell was employed for the cell fabrication. In the half-cell



Scheme 1. Flowchart of SnS nanoparticle synthesis.

configuration, the electrode was paired with lithium metal (reference/counter electrode) and separated using a glass microfiber separator (Whatman, cat no 1825-047, UK). For the full cell fabrication (LIB), the SnS half cell (Li/SnS) was fabricated initially and pre-treated electrochemically by discharging/charging for two cycles to eliminate the initial irreversibility and appropriate uniform solid electrolyte interface formation. In the case of LIC, the cells were pre-lithiated by three discharges to enable the formation ($\text{Li}_x\text{Sn} + \text{Li}_2\text{S}$), which was then dismantled inside the glove box and paired with the mass-balanced AC electrode to form the LIC full cell. Commercially available 1 M LiPF_6 in EC: DMC (1:1) was the electrolyte (Tomiyama, Japan) used in all the cell fabrication. The fabricated cells were subjected to electrochemical testing using a BioLogic battery tester (BCS-805) and Solartron electrochemical workstation (1470 E, UK).

3. Results and discussion

3.1. Material characterizations

The crystallinity and purity of the synthesized SnS nanoparticles were examined from the X-ray diffraction studies (Fig. 1a). The XRD peaks correspond to the orthorhombic crystal structure ($\alpha = \beta = \gamma = 90^\circ$) of SnS with space group $Pnma$ and has lattice parameters $a = 11.2$, $b = 3.9$, and $c = 4.3$ Å (DB card number: 01-075-2115). The crystallite size is calculated from the Debye-Scherrer equation (Equation E51), and the obtained average crystalline size of SnS is 8.8 nm. The post-cycling

structural changes were also evaluated, in which the Li/SnS cell was dismantled in the charged state ($\text{Sn}^0 + \text{Li}_2\text{S}$), and the XRD was recorded (Figure S1). It is observed from the pattern that the XRD peaks match with the standard Sn^0 and Li_2S peaks, confirming the phase formation. The texture of the SnS nanoparticles was analyzed using nitrogen adsorption/desorption studies (Figure S2). The sample has a high surface area of $119.6 \text{ m}^2 \text{ g}^{-1}$ with a pore radius of 14.8 Å and a pore volume of 0.18 mL g^{-1} , significantly enhancing the electrochemical performance by providing more active sites. The surface elemental composition and the redox state of the SnS nanoparticles were examined using the XPS survey, where we could observe peaks corresponding to Sn and S with no impurity element peak. The deconvoluted Sn 3d spectra (Fig. 1b) display peaks at binding energies 494.8 and 486.4 eV corresponding to the Sn $3d_{3/2}$ and Sn $3d_{5/2}$, inferring the Sn(II) state. In addition, the binding energy difference between the two peaks is around ~ 8.4 eV, which corresponds to the binding energy of the Sn 3d electron. The deconvoluted S 2p spectra (Fig. 1c) consist of two peaks at binding energies 162.1 and 160.95 eV corresponding to S $2p_{1/2}$ and S $2p_{3/2}$, respectively, indicating that the S element is in the reduced state (S^{2-}) [28,29]. Hence, it is confirmed from the XPS studies that the formed SnS phase is pure.

The morphological study and structural characterizations of the SnS sample were performed using the FE-SEM, TEM and HR-TEM analysis. The nano spherical morphology of SnS is evident from Fig. 2(a-c) but is observed in an agglomerated state. Meanwhile, post-mortem studies of the material show a different morphology with much more agglomeration (Figure S3(a-c)) because of the continuous alloying-dealloying

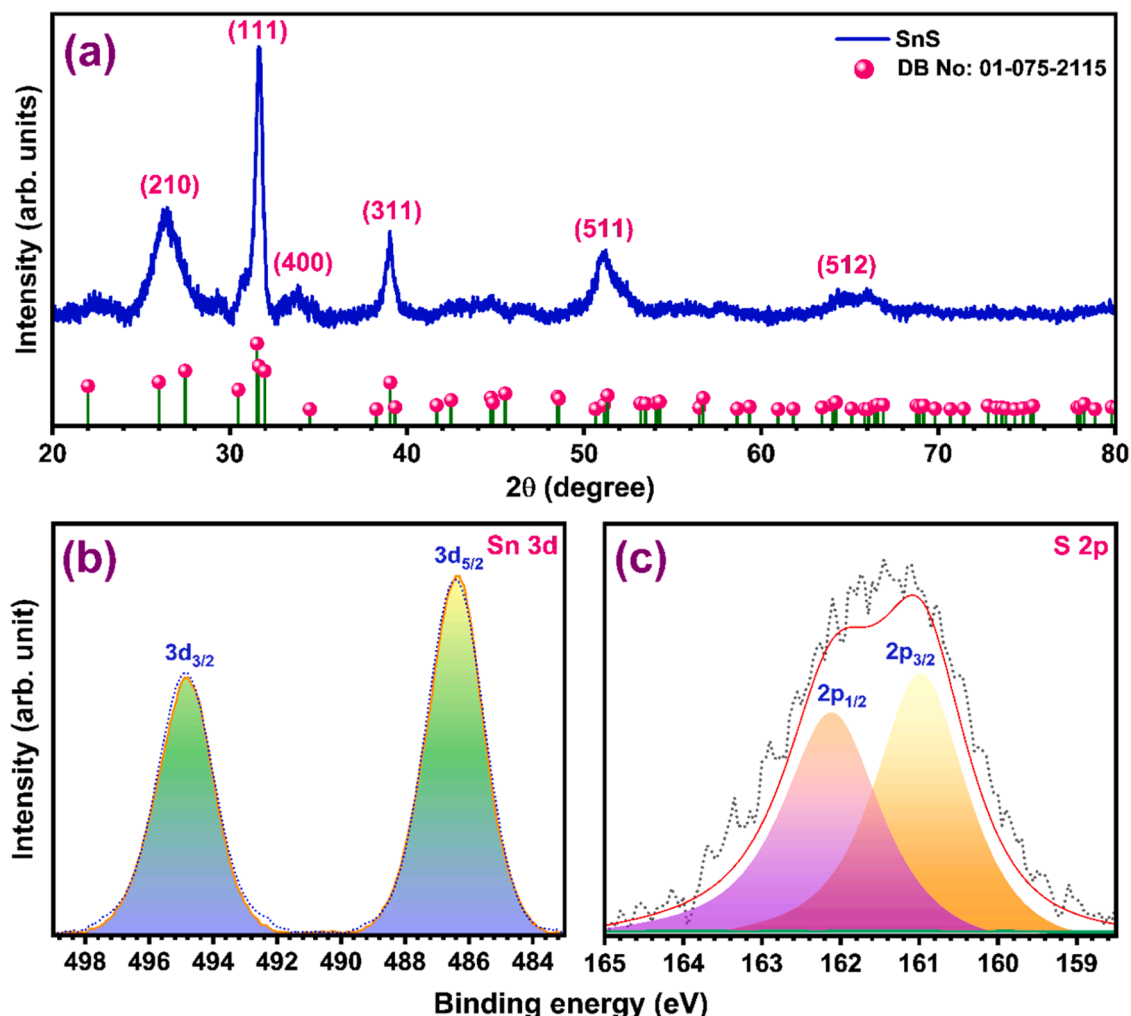


Fig. 1. Physical characterization of SnS nanoparticle: (a) XRD pattern, and (b-c) deconvoluted Sn 3d & S 2p XPS spectra.

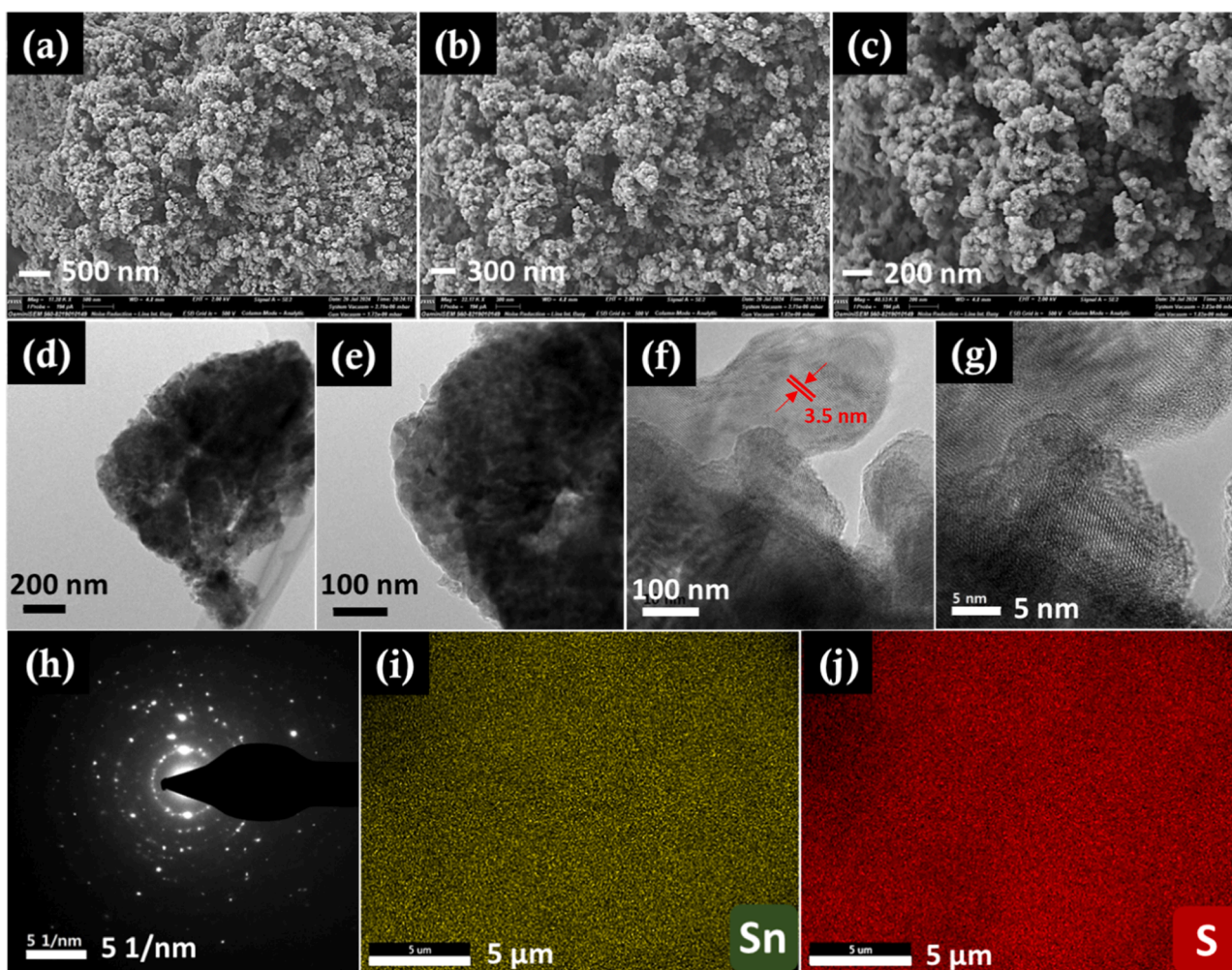


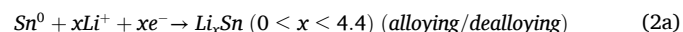
Fig. 2. Physical characterization of SnS: (a-c) FE-SEM images at different magnifications, (d & e) TEM images, (f & g) HR-TEM images, (h) SAED pattern, and (i & j) EDS elemental mapping.

during cycling. Fig. 2(d-g) displays the TEM and HR-TEM images, with the interplanar distance calculated from the image to be around 0.35 nm. The circular random dots in the SAED pattern in Fig. 2h also confirm the polycrystalline nature of the synthesized SnS nanoparticle. Further purity of the sample is validated from the EDS mapping (Fig. 2(i & j)), where tin and sulphur elements are only observed. Nevertheless, the post-cycling EDS mapping shows the presence of additional elements, such as carbon, oxygen, phosphorous and fluorine, which are added from the conductive carbon and electrolyte used in the cell fabrication (Figure S3d).

4. Electrochemical studies in half-cell assembly

As discussed in the experimental section, the electrochemical performance of the SnS electrode was examined in a CR2016-type coin cell setup using Li metal as reference/counter electrode and 1 M LiPF₆ in EC: DMC (1:1) as the electrolyte. The ability of SnS to store lithium ions is evaluated in half-cell assembly in galvanostatic and potentiostatic modes. The half-cell was initially subjected to cyclic voltammetric studies in the potential window 0.005 and 0.8 V vs. Li (Fig. 3a). Cyclic voltammogram (CV) curves display sharp cathodic peaks at 1.2 and 0.13 V vs. Li and a minor broad peak at 1.05 V vs. Li. The peaks at 1.2 and 1.05 V vs. Li indicate the conversion reaction of Sn²⁺ to Sn⁰ (Equation 1) and the electrolyte decomposition, respectively. These two are absent in the following cycles as we limited only to alloying/dealloying reaction with Li, indicated by the cathodic and anodic peaks at 0.13 and 0.5 V vs. Li,

respectively (Equation 2). In addition, the electrolyte decomposition is limited to the first cycle because of the robust SEI layer formed in the initial discharge, further validated from the *in-situ*-electrochemical impedance spectroscopic (*in-situ*-EIS) studies. There is only a peak on the anodic side of the cyclic voltammogram, as we have restricted to 0.8 V vs. Li to avoid further conversion reactions (i.e., Sn⁰ to Sn²⁺) affecting the stability of the cell [26,30,31].



The galvanostatic charge-discharge (GCD) is tested in the same potential window with lithium metal as the reference/counter electrode (Fig. 3b). The half-cell displayed an initial discharge capacity of 2038 mAh g⁻¹ and a reversible discharge capacity of 633 mAh g⁻¹ from the second cycle onwards. A huge decrease in capacity is observed from the first to the second cycle, which is mainly because of the structural decomposition of SnS and electrolyte decomposition in the initial discharge, resulting in the SEI layer formation, which agrees well with the CV studies. This is relatively common for the alloy anodes, especially limiting to the alloying reaction alone. However, from the second cycle, the higher coulombic efficiency is regained, and the cell displayed a specific capacity of 348 mAh g⁻¹ with >95 % coulombic efficiency after 100 cycles of charge-discharge (Fig. 3c). The half-cell was also subjected to rate performance studies at different current rates from 0.1 to 2 A g⁻¹, as shown in Fig. 3(d & e). A better cycling performance was exhibited by

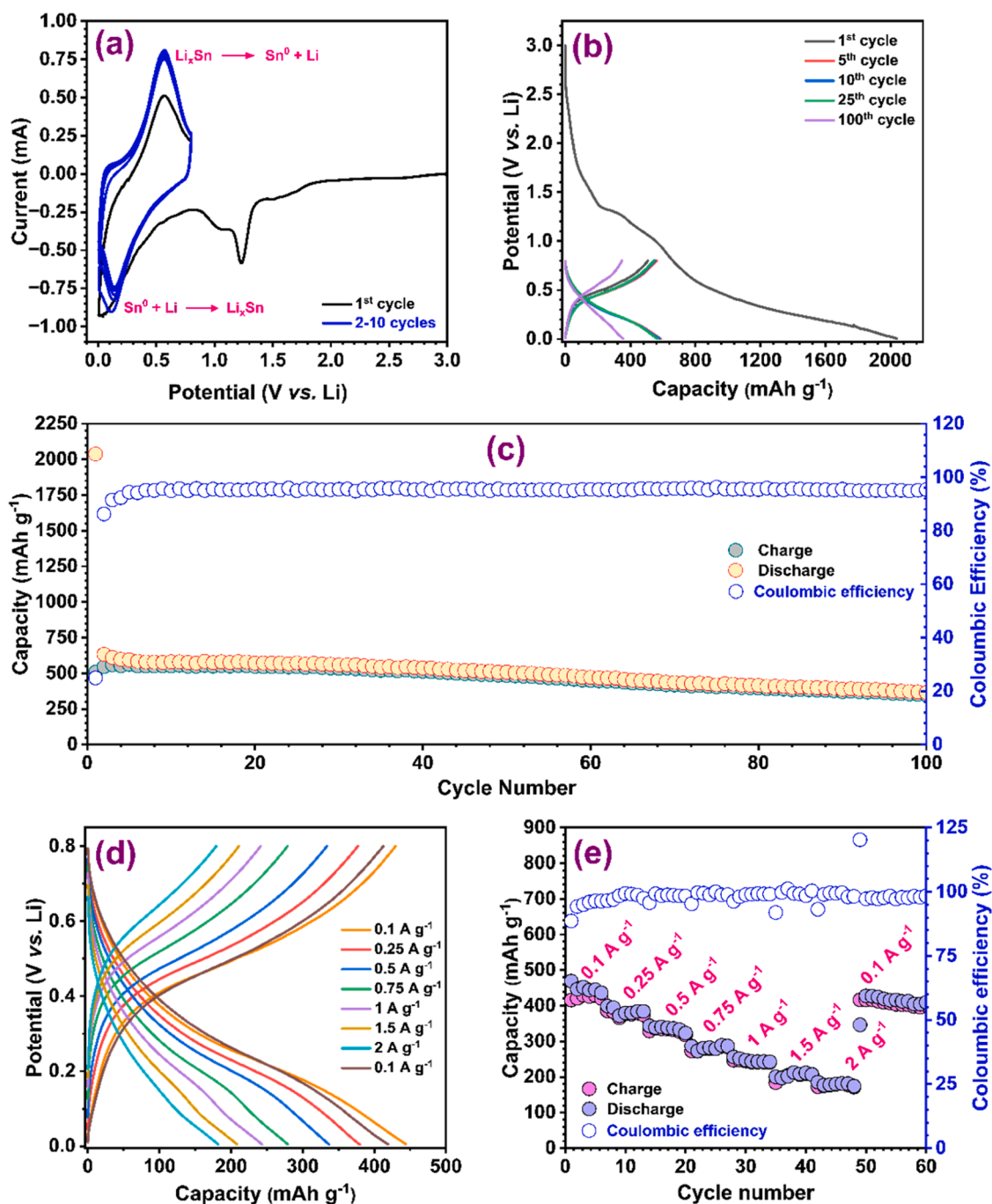


Fig. 3. Electrochemical performance of Li/SnS half cell: (a) Cyclic voltammogram at a scan rate of 0.1 mV s^{-1} , (b) galvanostatic charge-discharge at a current density of 0.1 A g^{-1} , (c) plot for capacity vs. cycle number, (d) GCD curves at different current rates, and (e) rate performance studies.

the half-cell at different current rates. We can observe a slight decrease in the specific capacity with an increase in the current rate, which is a commonly observed phenomenon irrespective of the nature of the electrode and mechanisms. However, when the current rate is returned to the lowest current rate, >94 % of the average discharge capacity is retained, which explains the stability and reversibility of the SnS electrode under the limited potential cycling.

The robustness of the SEI layer is important in determining the electrochemical performance of the alloying/conversion type anodes upon cycling. A strong and flexible SEI enhances the electrochemical performance and improves the cyclic stability. We have performed an *in-situ*-EIS study to analyze the SEI layer formation, strength and durability. The study continuously recorded the EIS at different potentials for each

cycle, and the representative traces of the 1st, 5th, 10th, 25th, and 50th cycles are displayed in Fig. 4. A higher charge-transfer resistance (R_{CT}) value is observed in the first discharge and charge, accounting for the SEI layer formation. However, from the 5th cycle to the 50th cycle, we could observe an almost stable R_{CT} value at all potentials, which clearly explains the robustness and stability of the SEI formed in the initial cycle. Based on the *in-situ*-EIS study, we strongly believe that a well-formed SEI layer on the SnS electrode surface has contributed significantly to stabilizing the cell upon prolonged cycling.

The cathodes utilized in the LIB and LIC assemblies are $\text{LiNi}_{0.5}\text{Mn}_{1.5}\text{O}_4$ and AC, respectively. The $\text{LiNi}_{0.5}\text{Mn}_{1.5}\text{O}_4$ half-cells are fabricated by pairing it with Li metal and are tested in the potential window of 3.5 to 5 V vs. Li (Figure S4 (a & c)). The cell displayed an

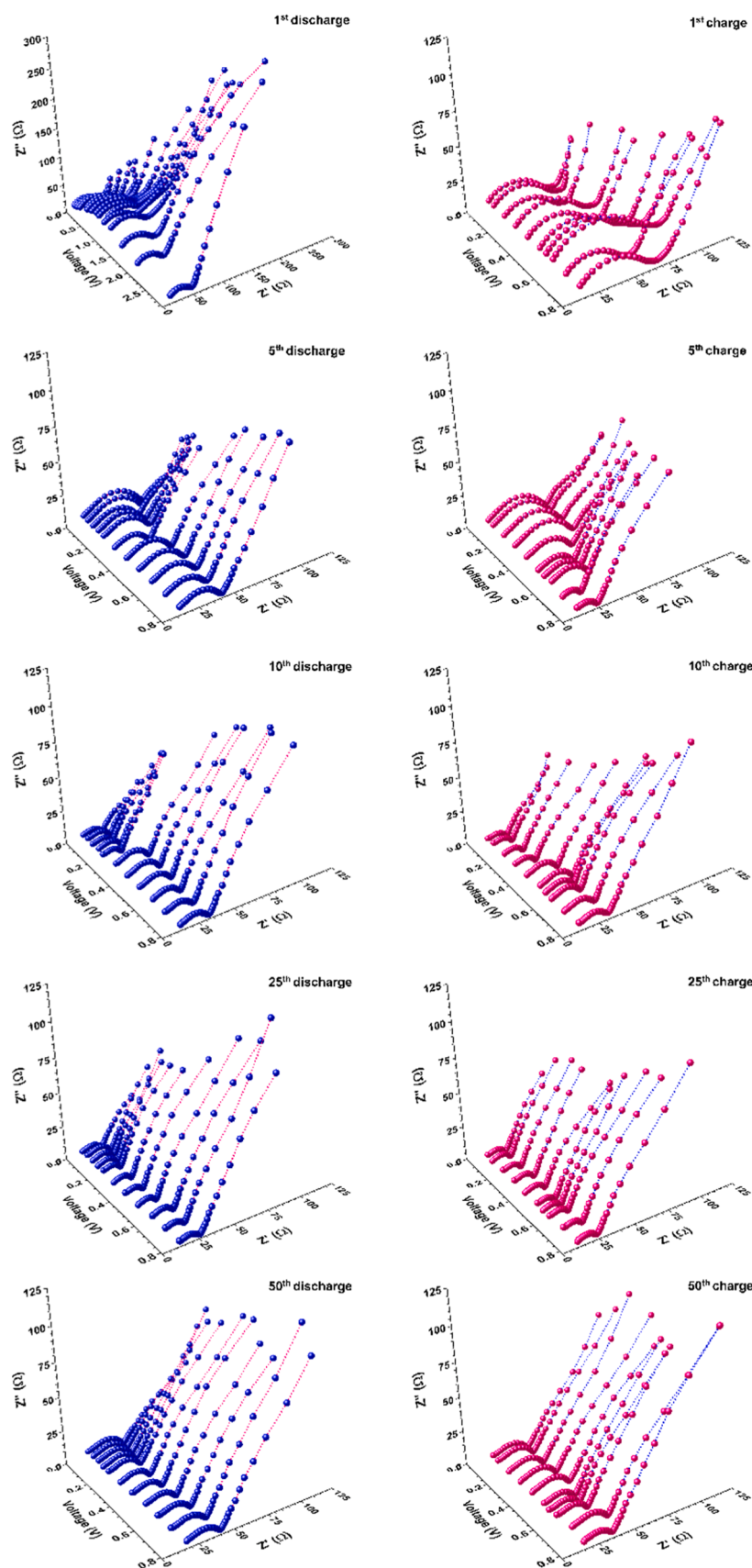


Fig. 4. In-situ-electrochemical impedance spectroscopic profile of Li/SnS half-cell with traces of 1st, 5th, 10th, 25th, and 50th cycles.

initial discharge capacity of 131 mAh g^{-1} and retained a capacity of 121 mAh g^{-1} after 200 cycles. The AC half-cells, on the other hand, are tested from 1.5 to 4.5 V vs. Li, with the cell exhibiting an initial discharge capacity of 144 mAh g^{-1} and capacity retention of 127 mAh g^{-1} after 350 cycles (Figure S5 (b & d)). In the case of the $\text{LiNi}_{0.5}\text{Mn}_{1.5}\text{O}_4$ cathode, the energy is stored via a Faradaic reaction, whereas for the AC cathode, a simple non-Faradaic adsorption/desorption of cations/anions happens during charge/discharge process which is clearly evident from the shape and nature of the curves [32,33].

5. Electrochemical full-cell studies

The full-cells are fabricated by pairing the pre-treated/lithiated anode with the mass-balanced cathode. In our study, we tested the SnS's performance in both LIB and LIC. For both full-cell fabrication and electrochemical pre-treated/lithiated, the Li/SnS half-cell is initially fabricated and electrochemically pre-treated by cycling for a few cycles to mitigate the irreversible capacity loss and subsequently paired with $\text{LiNi}_{0.5}\text{Mn}_{1.5}\text{O}_4$ cathode. For the case of LIC, the cell at the pre-lithiated state, i.e., discharged state ($\text{Li}_x\text{Sn} + \text{Li}_2\text{S}$), de-crimped and paired with

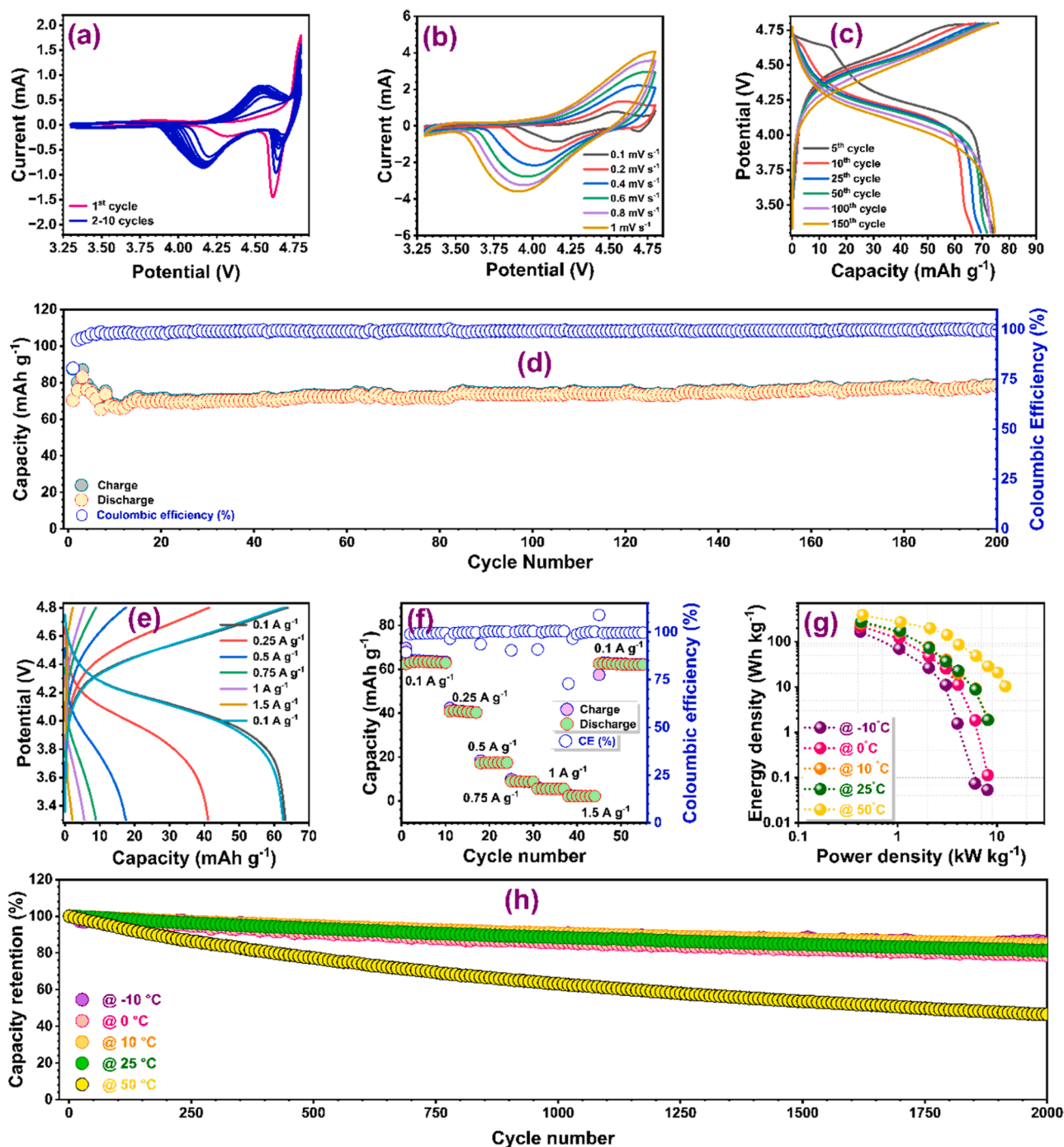


Fig. 5. Electrochemical performance of LNMO//SnS LIB: (a) Cyclic voltammogram at a scan rate of 0.1 mV s^{-1} , (b) CV traces at different scan rates, (c) galvanostatic charge-discharge at a current density of 0.1 A g^{-1} , (d) plot for capacity vs. cycle number, (e) GCD at different current rates, (f) capacity at different current rates, (g) Ragone plot comparing energy and power densities at different current rates and temperatures, and (h) capacity retention vs. cycle number plot at different temperatures.

the mass-balanced cathode to obtain the full cell. Mass balancing is an essential step in full-cell fabrication and is performed by the equation given in the supplementary section (Equation E₅2). The mass-balanced cathode, $\text{LiNi}_{0.5}\text{Mn}_{1.5}\text{O}_4$ or AC, is paired with a pre-treated/lithiated SnS electrode to fabricate the LIB or LIC, respectively.

LNMO//SnS Full-cell: The LIB is subjected to various electrochemical studies in the potential window 3.3 to 4.8 V. Fig. 5a displays the CV traces of the LIB at a scan rate of 0.1 mV s^{-1} , with the cathodic peaks at 4.6, and 4.1 V and anodic peak at 4.79, and 4.5 V, indicating the simultaneous redox reactions of both LNMO and SnS. In addition, the CV

was also performed at different scan rates from 0.1 to 1 mV s^{-1} , as shown in Fig. 5b. The LIB was also subjected to GCD studies in the same potential window at a current rate of 0.1 A g^{-1} (Fig. 5(c& d)). The cell exhibited an initial specific capacity of 87 mAh g^{-1} and stable cycling performance for >200 cycles. The full-cell has a specific capacity of 78 mAh g^{-1} with a high coulombic efficiency of $>99\%$ after 200 cycles. The cell was also subjected to rate performance studies at different current rates from 0.1 to 1.5 A g^{-1} (Fig. 5e). As expected, the specific capacity decreased with an increase in the current rate due to the inability to provide sufficient time for the complete reaction. Still, it is interesting to

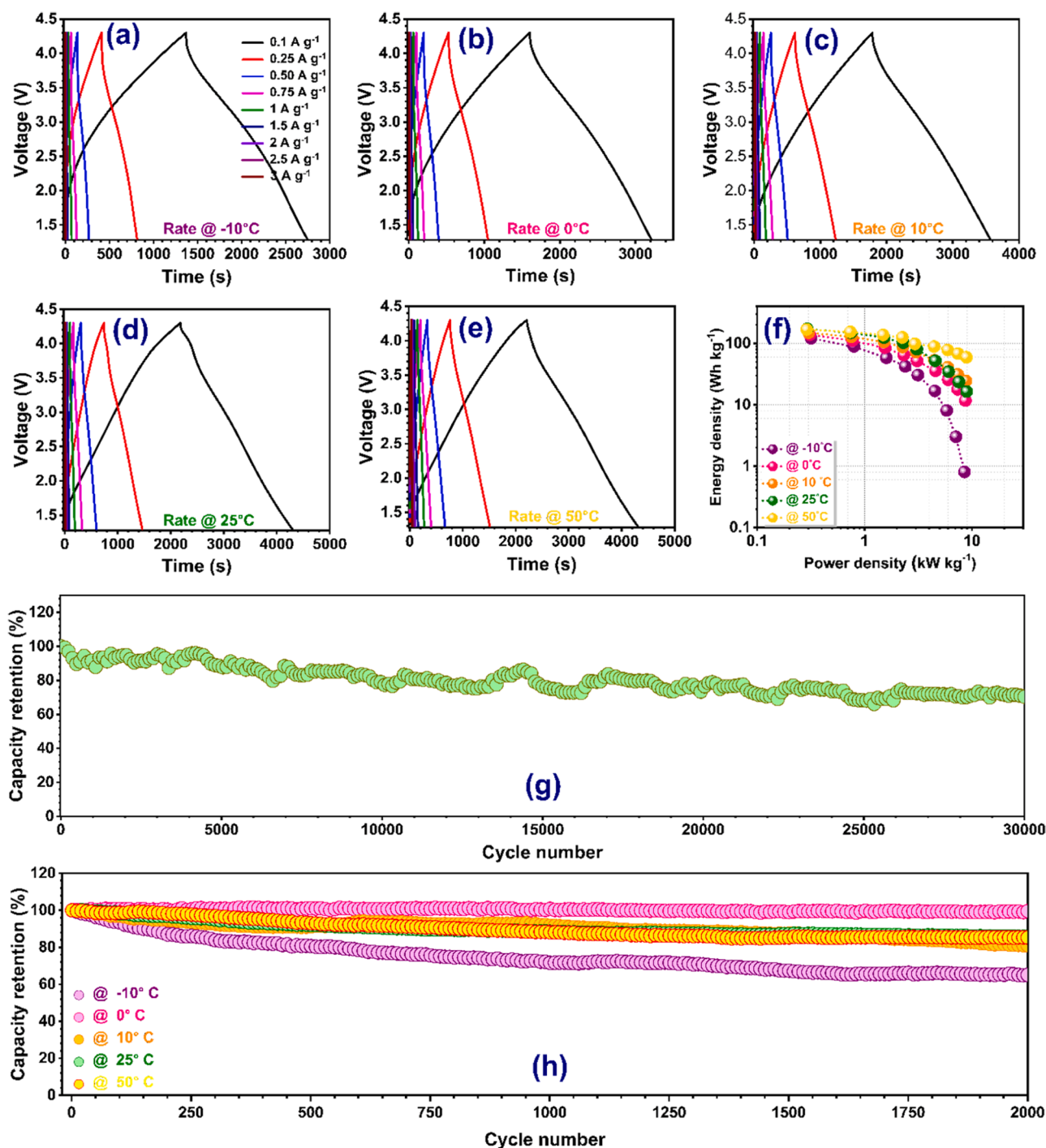


Fig. 6. Electrochemical performance of AC//SnS LIC: (a-e) E_{cell} vs. time plot at different temperatures, (f) Ragone plot comparing energy and power density values at different current rates and temperatures, (g) long-term cycling profile at room temperature conditions at a current density of 1 A g^{-1} , and (h) long-term cycling at different temperatures.

note the high reversibility of the cell as the LIB retained >98 % of the average specific capacity when the current rate was again reduced to the lower rate (Fig. 5f). Fig. 5g, the Ragone plot, gives us the LIB's energy and power density values. The LIB with 1.68 mg (1.48 mg cm^{-2}) and 6.84 mg (4.4 mg cm^{-2}) anodic and cathodic mass delivered a maximum energy density of $\sim 272 \text{ Wh kg}^{-1}$ and a power density of $\sim 8.1 \text{ kW kg}^{-1}$ at room temperature. The LIB displayed even higher energy and power density values when tested at different temperature conditions (-10 , 0 , 10 , 25 and 50°C).

A maximum energy density of $\sim 387 \text{ Wh kg}^{-1}$ and power density of $\sim 12.2 \text{ kW kg}^{-1}$ was obtained at 50°C . The increased activity of the electrolyte at higher temperatures enhanced the diffusion of Li^+ ions, thereby elevating the energy and power of the LIB. At other temperature conditions, reasonable energy and power density values were attained. The long-term cycling analysis was also performed for over 2000 cycles at various temperatures (Fig. 5h). Except for 50°C , the capacity retention after 2000 cycles was either close to or above 80 %. In the case of higher temperatures, the increased electrolytic activity catalyzed the side reactions and reduced the cycling life.

AC//SnS Full-cell: A fabrication method similar to LIB is adopted in LIC, but instead of pre-treated SnS, the electrochemically pre-lithiated form is used as a negative electrode ($\text{Li}_x\text{Sn} + \text{Li}_2\text{S}$). First, a CV analysis is performed for the full-cell from 1.3 to 4.3 V at different scan rates, given in Figure S5. This quasi-rectangular-shaped CV represents the hybrid nature of the two different electrodes and mechanisms involved in the charge storage process of LIC. The GCD was performed for the LIC at different current rates (0.1 to 3 A g^{-1}) for various temperature conditions to evaluate the LIC's performance at various atmospheric conditions. The E_{cell} vs. time graph from -10 to 50°C is given in Fig. 6 (a-e). The LIC's energy and power density values are calculated based on the total mass loading of the anode (1.6 mg , 1.4 mg cm^{-2}) and cathode (5.23 mg , 3.4 mg cm^{-2}), respectively, are calculated from the Ragone plot in Fig. 6f. The full cell displayed a maximum energy and power density of $\sim 172 \text{ Wh kg}^{-1}$ and 8.9 kW kg^{-1} at room temperature. The LIC has satisfactory energy and power at other temperatures but slightly less than at room temperature. This work was also compared with the previously reported works where carbonaceous and alloy-type anodes were used in LIC assembly. From the Ragone plot given in Figure S6, we get a clear picture of the excellent electrochemical performance of the present work. The table in Table S1 also compares this work's energy/power values with the previously reported ones. The long-term cycling analysis of the AC//($\text{Li}_x\text{Sn} + \text{Li}_2\text{S}$) LIC was analyzed at room temperature for over 30,000 cycles (Fig. 6g). We could observe nearly 80 % of the capacity being retained even after cycling for 20,000 cycles, which opens the door toward its practical application. In addition to the room temperature, the long-term cycling analysis was performed at different temperatures, from lowest -10 to highest 50°C (Fig. 6h). It is noteworthy that after 2000 cycles, over 80 % of the capacity is retained at all temperatures except for -10°C . The freezing of electrolytes at lower temperatures resulted in the degradation in cycling performance at -10°C .

From the analysis of electrochemical studies performed for both the LIB and LIC, we could conclude that the SnS is one of the best anode materials with the potential to replace the prevailing graphitic anode in the market. LIB & LIC exhibited exceptionally higher energy and power density values at different temperatures, making them suitable candidates for different climatic applications. We strongly believe that limiting the potential window of the alloy anode, especially SnS, is one of the crucial factors in enabling stable cycling performance. Also, balanced mass loading, suitable potential window and appropriate electrochemical pre-treatment/pre-lithiation are worth mentioning for the exceptional performance of both cells. Furthermore, the optimization of SnS material in terms of synthesis and electrochemical studies is in progress to enhance the Li-ion storage performance of the material and to analyze the possibility of upscaling for industrial application and commercialization.

6. Conclusion

In our work, we have synthesized SnS nanoparticles using the single-step co-precipitation method and explored its possibility as an alloy-type anode for the Lithium-ion battery/capacitor, limiting its potential window. The SnS half-cells displayed excellent long-term cycling and rate performance when paired with metallic lithium. The nanosize and its morphology contributed to the stable SEI layer formation and enhanced the electrochemical performance. The interfacial properties and robustness/steadiness of the SEI were evaluated in the *in-situ*-EIS studies, concluding that strong SEI is one of the primary reasons for the improved cycling performance. The LIB displayed an exceptional maximum energy density of 387 Wh kg^{-1} with long-term cycling for >200 cycles with high-capacity retention. On the other hand, the LIC exhibited a maximum energy density and power density of 172 Wh kg^{-1} and 8.9 kW kg^{-1} , respectively, with ultra-long cycling performance for >30,000 cycles. The functioning of LIB and LIC at different climatic conditions was evaluated by testing the full cells in different temperature conditions from the lowest of -10°C to the maximum of 50°C . The battery and hybrid capacitor displayed excellent rate and long-term performance for over 2000 cycles at all temperatures. Overall, the SnS is one of the best alloying-type anodes for both LIB & LIC, and further research is in progress to enhance its performance for scaling up as a commercial anode.

CRedit authorship contribution statement

Manohar Akshay: Writing – review & editing, Writing – original draft, Validation, Project administration, Data curation, Conceptualization. **Yun-Sung Lee:** Writing – review & editing, Writing – original draft, Validation, Project administration, Data curation, Conceptualization. **Vanchiappan Aravindan:** Writing – review & editing, Writing – original draft, Validation, Project administration, Data curation, Conceptualization.

Declaration of competing interest

The authors declare that they have no known competing financial interests or personal relationships that could have appeared to influence the work reported in this paper.

Acknowledgement

YSL acknowledges the financial support from the National Research Foundation of Korea (NRF) grant funded by the Korean government (Ministry of Science, ICT & Future Planning) (No. RS-2023-00208361). VA acknowledges financial support from the Anusandhan National Research Foundation (ANRF), Govt. of India, through Swarnajayanti Fellowship (SB/SJF/2020–21/12).

Supplementary materials

Supplementary material associated with this article can be found, in the online version, at [doi:10.1016/j.electacta.2025.147385](https://doi.org/10.1016/j.electacta.2025.147385).

Data availability

Data will be made available on request.

References

- [1] A. Barré, B. Deguilhem, S. Grolleau, M. Gérard, F. Suard, D.A. Riu, Review on lithium-ion battery ageing mechanisms and estimations for automotive applications, *J. Power. Sourc.* 241 (2013) 680–689, <https://doi.org/10.1016/j.jpowsour.2013.05.040>.

- [2] T. Kim, W. Song, D.Y. Son, L.K. Ono, Y. Qi, Lithium-ion batteries: outlook on present, future and hybridized technologies, *J. Mater. Chem. A* 7 (7) (2019) 2942–2964, <https://doi.org/10.1039/C8TA10513H>.
- [3] A. González, E. Goikolea, J.A. Barrena, R. Mysyk, Review on supercapacitors: technologies and materials, *Renew. Sustain. Energy. Rev.* 58 (2016) 1189–1206, <https://doi.org/10.1016/j.rser.2015.12.249>.
- [4] Poonam, K. Sharma, A. Arora, S.K. Tripathi, Review of supercapacitors: materials and devices, *J. Energy. Storage.* 21 (2019) 801–825, <https://doi.org/10.1016/j.est.2019.01.010>.
- [5] M. Yaseen, M.A.K. Khattak, M. Humayun, M. Usman, S.S. Shah, S. Bibi, B.S. U. Hasnain, S.M. Ahmad, A. Khan, N. Shah, A.A. Tahir, H. Ullah, A review of supercapacitors: materials design, modification, and applications, *Energies* 14 (22) (2021), <https://doi.org/10.3390/en14227779>.
- [6] V. Aravindan, J. Gnanaraj, Y.S. Lee, S. Madhavi, Insertion-type electrodes for nonaqueous Li-ion capacitors, *Chem. Rev.* 114 (23) (2014) 11619–11635, <https://doi.org/10.1021/cr5000915>.
- [7] S. Zhao, X. Sun, N. Wang, C. Li, Y. An, Y. Xu, K. Wang, X. Zhang, Y. Ma, Recent advances in hybrid lithium-ion capacitors: materials and processes, *ACS. Appl. Energy. Mater.* (2024), <https://doi.org/10.1021/acsaem.4c00230>.
- [8] H. Wang, C. Zhu, D. Chao, Q. Yan, H.J. Fan, Nonaqueous hybrid lithium-ion and sodium-ion capacitors, *Adv. Mater.* 29 (46) (2017) 1702093, <https://doi.org/10.1002/adma.201702093>.
- [9] A. Jagade, X. Zhou, R. Xiong, D.P. Dubal, J. Xu, S. Yang, Lithium ion capacitors (LICs): development of the materials, *Energy. Storage. Mater.* 19 (2019) 314–329, <https://doi.org/10.1016/j.ensm.2019.02.031>.
- [10] S. Yuan, Q. Lai, X. Duan, Q. Wang, Carbon-based materials as anode materials for lithium-ion batteries and lithium-ion capacitors: a review, *J. Energy. Storage* 61 (2023) 106716, <https://doi.org/10.1016/j.est.2023.106716>.
- [11] W. Zhao, C. Zhao, H. Wu, L. Li, C. Zhang, Progress, challenge and perspective of graphite-based anode materials for lithium batteries: a review, *J. Energy. Storage* 81 (2024) 110409, <https://doi.org/10.1016/j.est.2023.110409>.
- [12] J. Asenbauer, T. Eisenmann, M. Kuenzel, A. Kazzazi, Z. Chen, D. Bresser, The success story of graphite as a lithium-ion anode material-fundamentals, remaining challenges, and recent developments including silicon (Oxide) composites, *Sustain. Energy. Fuels* 4 (11) (2020) 5387–5416, <https://doi.org/10.1039/d0se00175a>.
- [13] Manohar, A.; Viswanathan, A.; Yun-Sung, L.; Aravindan, V. All-in-All: dead lithium-ion battery to active lithium-ion capacitor. *ChemSusChem*. n/a (n/a), e202400449. <https://doi.org/10.1002/cssc.202400449>.
- [14] M. Akshay, S. Jyothilakshmi, Y.S. Lee, V. Aravindan, High-performance Li-ion and Na-ion capacitors based on a spinel $\text{Li}_4\text{Ti}_5\text{O}_{12}$ anode and carbonaceous cathodes, *Small*. 20 (15) (2024) 2307248, <https://doi.org/10.1002/sml.202307248>.
- [15] V. Aravindan, Y.S. Lee, Building next-generation Li-ion capacitors with high energy: an approach beyond intercalation, *J. Phys. Chem. Lett.* 9 (14) (2018) 3946–3958, <https://doi.org/10.1021/acs.jpclett.8b01386>.
- [16] M. Akshay, K. Subramanyan, M.L. Divya, Y.S. Lee, V. Aravindan, Choice of binder on conversion type CuO nanoparticles toward building high energy Li-ion capacitors: an approach beyond intercalation, *Adv. Mater. Technol.* 7 (9) (2022) 2200423, <https://doi.org/10.1002/admt.202200423>.
- [17] M. Akshay, R. Belgamwar, S. Praneetha, V. Polshettiwar, V. Aravindan, Defect engineered dendritic fibrous nanosilica as prospective alloy anode for the fabrication of high-energy Li-ion capacitors with ultralong durability, *ACS. Mater. Lett.* (2023) 715–721, <https://doi.org/10.1021/acsmaterialslett.2c01224>.
- [18] H. Zhang, I. Hasa, S. Passerini, Beyond insertion for Na-ion batteries: nanostructured alloying and conversion anode materials, *Adv. Energy. Mater.* 8 (17) (2018) 1702582, <https://doi.org/10.1002/aenm.201702582>.
- [19] M. Akshay, S. Jayaraman, M. Ulaganathan, Y.S. Lee, V. Aravindan, Interphase stabilized electrospun SnO_2 fibers as alloy anode via restricted cycling for Li-ion capacitors with high energy and wide temperature operation, *J. Colloid. Interface. Sci.* 646 (May) (2023) 703–710, <https://doi.org/10.1016/j.jcis.2023.05.091>.
- [20] Y. Han, G. Huang, S. Xu, Structural reorganization–Based nanomaterials as anodes for lithium-ion batteries: design, preparation, and performance, *Small* 16 (15) (2020) 1902841, <https://doi.org/10.1002/sml.201902841>.
- [21] M. Akshay, S. Praneetha, Y.S. Lee, V. Aravindan, Hierarchical SnO_2 @PC@PANI composite via In-situ polymerization towards next-generation Li-ion capacitor by limiting alloying process with high energy, wide temperature performance, and cyclability, *Electrochim. Acta.* 439 (2023) 141599, <https://doi.org/10.1016/j.electacta.2022.141599>.
- [22] Y. Shan, Y. Li, H. Pang, Applications of tin sulfide-based materials in lithium-ion batteries and sodium-ion batteries, *Adv. Funct. Mater.* 30 (23) (2020) 1–31, <https://doi.org/10.1002/adfm.202001298>.
- [23] S. Feng, L. Ma, J. Lin, X. Lu, L. Xu, J. Wu, X. Yan, X. Fan, SnS nanoparticles anchored on nitrogen-doped carbon sheets derived from metal-organic-framework precursors as anodes with enhanced electrochemical sodium ions storage, *Electrochim. Acta.* 387 (2021) 138535, <https://doi.org/10.1016/j.electacta.2021.138535>.
- [24] J. Huang, J. Chen, L. Ma, Q. Liu, M. Wang, L. Liao, T. Rujiralai, L. Xu, In-situ coupling SnS with nitrogen-doped porous carbon for boosting Li-storage in lithium-ion battery and capacitor, *Electrochim. Acta.* 365 (2021) 137350, <https://doi.org/10.1016/j.electacta.2020.137350>.
- [25] L. Xu, L. Ma, X. Zhou, Y. Ling, X. Wang, M. Chen, Hierarchical flower-like SnS grafted with glucosamine-derived nitrogen-doped carbon with enhanced reversible Li-storage performance, *Appl. Surf. Sci.* 458 (2018) 86–94, <https://doi.org/10.1016/j.apsusc.2018.07.082>.
- [26] Y. Cheng, Y. Cheng, Z. Wang, L. Chang, S. Wang, Q. Sun, Z. Yi, Z. Yi, L. Wang, L. Wang, Sulfur-mediated interface engineering enables fast SnS nanosheet anodes for advanced lithium/sodium-ion batteries, *ACS. Appl. Mater. Interfaces.* 12 (23) (2020) 25786–25797, <https://doi.org/10.1021/acsaami.0c03860>.
- [27] B. Zhao, D. Song, Y. Ding, J. Wu, Z. Wang, Z. Chen, Y. Jiang, J. Zhang, Ultrastable Li-ion battery anodes by encapsulating SnS nanoparticles in sulfur-doped graphene bubble films, *Nanoscale* 12 (6) (2020) 3941–3949, <https://doi.org/10.1039/c9nr10608a>.
- [28] R.K. Yadav, P.S. Pawar, Y.T. Kim, I. Sharma, J. Heo, Prebaking of an SnS source with sulfur for achieving higher photovoltaic performance in VTD- SnS thin films for solar cells, *J. Mater. Chem. A* 12 (6) (2024) 3265–3275, <https://doi.org/10.1039/D3TA05204D>.
- [29] M. Choi, W. William, J. Hwang, D. Yoon, J. Kim, A supercritical ethanol route for one-pot synthesis of tin sulfide-Reduced graphene oxides and their anode performance for lithium ion batteries, *J. Ind. Eng. Chem.* 59 (2018) 160–168, <https://doi.org/10.1016/j.jiec.2017.10.020>.
- [30] Z. Wei, L. Wang, M. Zhuo, W. Ni, H. Wang, J. Ma, Layered tin sulfide and selenide anode materials for Li- and Na-ion batteries, *J. Mater. Chem. A* 6 (26) (2018) 12185–12214, <https://doi.org/10.1039/c8ta02695e>.
- [31] S.H. Yu, A. Jin, X. Huang, Y. Yang, R. Huang, J.D. Brock, Y.E. Sung, H.D. Abruna, SnS/C nanocomposites for high-performance sodium ion battery anodes, *RSC. Adv.* 8 (42) (2018) 23847–23853, <https://doi.org/10.1039/c8ra04421j>.
- [32] S. Subhadarshini, N.K. Peyada, D.K. Goswami, N.C. Das, Review of battery-type transition metal (Cu, Co, and Ni) oxide based electrodes: from fundamental science to fabrication of a hybrid supercapacitor device, *Energy. Fuels.* 38 (13) (2024) 11455–11493, <https://doi.org/10.1021/acs.energyfuels.4c01460>.
- [33] Q. Guo, N. Chen, L. Qu, The advance and perspective on electrode materials for metal-Ion hybrid capacitors, *Adv. Energy. Sustain. Res.* 2 (7) (2021), <https://doi.org/10.1002/aesr.202100022>.